

# SCIENTIFIC REPORTS



OPEN

## Enhancement of perpendicular magnetic anisotropy and its electric field-induced change through interface engineering in Cr/Fe/MgO

A. Koziol-Rachwał<sup>1,2</sup>, T. Nozaki<sup>1</sup>, K. Freindl<sup>3</sup>, J. Korecki<sup>2,3</sup>, S. Yuasa<sup>1</sup> & Y. Suzuki<sup>1,4</sup>

Recently, perpendicular magnetic anisotropy (PMA) and its voltage control (VC) was demonstrated for Cr/Fe/MgO. In this study, we shed light on the origin of large voltage-induced anisotropy change in Cr/Fe/MgO. Analysis of the chemical structure of Cr/Fe/MgO revealed the existence of Cr atoms in the proximity of the Fe/MgO interface, which can affect both magnetic anisotropy (MA) and its VC. We showed that PMA and its VC can be enhanced by controlled Cr doping at the Fe/MgO interface. For Cr/Fe (5.9 Å)/Cr (0.7 Å)/MgO with an effective PMA of 0.8 MJ/m<sup>3</sup>, a maximum value of the voltage-controlled magnetic anisotropy (VCMA) effect of 370 fJ/Vm was demonstrated due to Cr insertion.

Development of high density non-volatile memories that provide fast access and low energy consumption is crucial for next generation spintronics. Manipulation of magnetization by electric currents has recently attracted a lot of interests due to its application in magnetic random access memory (MRAM)<sup>1</sup>. Current-induced magnetization switching through spin transfer torque (STT) is one of the promising candidates for a novel writing technique in MRAM<sup>2</sup>. Low writing energy of the order of 100fJ/bit with good scalability was realized by recent STT technology, however, electric-current based manipulations still require reduction of unwanted energy loss caused by the Ohmic dissipation. Recently, electric field-controlled magnetic effects have attracted attention due to their potential application in high density, low power-consumption memories. With a use of voltage-controlled magnetic storage, an Ohmic dissipation, which is the predominant loss mechanism in magnetic memories, can be significantly reduced to the order of a few fJ/bit<sup>3</sup>.

Various studies on voltage-controlled magnetic effects have been reported for different materials, including ferromagnetic (FM) semiconductors, FM metals, or multiferroics (for review see ref. 4 and Ref. within). For FM metals the VC of magnetism via electrical modulation of magnetic anisotropy (MA)<sup>5,6</sup>, the Curie temperature<sup>7</sup>, domain wall motion<sup>8–10</sup>, and the interfacial asymmetric exchange interaction<sup>11</sup> have been demonstrated so far. Moreover, recent reports on electrically-induced spin reorientation transition<sup>12</sup>, bistable magnetization switching<sup>13–15</sup>, and excitation of high frequency magnetization dynamics in an ultrathin FeCo layer by using the VC of MA<sup>16,17</sup> have contributed to the realization of a new class of voltage-controlled magnetoresistive random access memory (MRAM)<sup>18</sup>. Furthermore, according to the experimental and theoretical studies the VCMA effect can be used to provide an ultralow energy current-induced magnetization switching in magnetic tunnel junctions<sup>18,19</sup>.

For FM metal films, in contrast to semiconductors<sup>20</sup>, the voltage-induced changes in magnetism are restricted to the atoms closest to the surface due to the short screening length. Several mechanisms have been proposed to be responsible for the voltage-controlled magnetic anisotropy (VCMA) in FM systems. Theoretical studies attributed the origin of the VCMA effect to the spin-dependent screening of the electric field in FM layers<sup>21</sup> or the change in the relative occupancy of the orbitals of atoms at the interface related to the accumulation/depletion of electrons<sup>22–24</sup>. Also, a discussion of VCMA effect in relation to the intrinsic dipole field existing at the Fe/MgO interface was presented recently<sup>25</sup>. Experimentally, changes in perpendicular magnetic anisotropy (PMA) under an electric field ranges between tenths to thousands of fJ/Vm. The biggest variations of the areal density of

<sup>1</sup>National Institute of Advanced Industrial Science and Technology, Spintronics Research Center, Tsukuba, Ibaraki, 305-8568, Japan. <sup>2</sup>Faculty of Physics and Applied Computer Science, AGH University of Science and Technology, al. Mickiewicza 30, 30-059, Kraków, Poland. <sup>3</sup>Jerzy Haber Institute of Catalysis and Surface Chemistry, Polish Academy of Sciences, ul. Niezapominajek 8, 30-239, Kraków, Poland. <sup>4</sup>Graduate School of Engineering Science, Osaka University, 1-3 Machikaneyama, Toyonaka, Osaka, 560-8531, Japan. Correspondence and requests for materials should be addressed to A.K.-R. (email: [akoziol@agh.edu.pl](mailto:akoziol@agh.edu.pl))

the anisotropy energy under an electric field (the so-called VCMA coefficient) were demonstrated for systems in which voltage-induced redox reactions<sup>26</sup>, charge trapping effects<sup>27</sup>, electromigration<sup>28</sup>, or magnetostriction<sup>29</sup> were involved. Although the above-mentioned effects can contribute to the VCMA coefficients being as high as a few thousand fJ/Vm, a practical application of the systems for which VCMA is related to chemical reactions at the interface or magnetostriction is limited due to the low operating speed and poor write endurance. However, from a practical point of view, the systems for which the VCMA effect mainly originates from modifications of the electronic structure seems to be promising due to the high-speed operation. Aside from a large VCMA effect, a large PMA is desired to satisfy high thermal stability at reduced dimensions. Since both the VCMA effect and PMA usually have interfacial origins, the growth of high quality and controllable metal/dielectric interfaces is crucial for the understanding and further development of systems that exhibit voltage-tunable MA.

Recently, high interfacial MA<sup>30–32</sup> and a large VCMA effect<sup>33</sup> were found in an ultrathin Fe layer embedded between Cr and MgO. For an Fe layer with nominal thickness greater than 6 Å a high interfacial anisotropy of 2.1 mJ/m<sup>2</sup> and a linear VCMA coefficient of about 100 fJ/Vm were observed. For Fe layers thinner than 6 Å, a considerable reduction in PMA and the saturation magnetization ( $M_s$ ) were noted. A reduction of the Curie temperature ( $T_c$ ) could be responsible for this behavior<sup>34</sup>. However, in our studies even for very thin Fe layers we did not observe a strong dependence in  $M_s$  as a function of temperature that appears close to  $T_c$ <sup>33</sup>. Another possible origin of reduction of the  $M_s$  value can be an intermixing between Fe and Cr<sup>35</sup>.

Fe/Cr intermixing can occur especially when an annealing treatment is used during the deposition process<sup>36</sup>. Interestingly, for the thickness of the Fe layer for which a reduction in PMA and  $M_s$  were noted, a large VCMA coefficient was observed. For a nominal thickness of the Fe layer of 5.3 Å, a VCMA coefficient of 290 fJ/Vm was obtained under a negative voltage, while the PMA remained almost unchanged under a positive voltage. These results suggest that for a deeper understanding of the origin of PMA and its VC, the chemical structure of Cr/Fe/MgO should be analyzed in detail.

In the first part of this paper, we discuss an experimental verification of the local atomic structure of the Cr/<sup>57</sup>Fe/MgO, where the <sup>57</sup>Fe isotope enabled the use of conversion electron Mössbauer spectroscopy (CEMS). We show the effects of annealing after the deposition of the MgO barrier on the magnetic properties and chemical structure in the system. We demonstrate that although no heavy intermixing exists between Fe and Cr in Cr/Fe/MgO, Cr impurities exist at the Fe/MgO interface after annealing. These Cr atoms in the proximity of the Fe/MgO interface can influence the PMA and VCMA.

Inspired by the CEMS results, in the second part of the paper we investigated the role of the insertion of an ultrathin Cr layer at the Fe/MgO interface on PMA and its voltage-induced change in Cr/Fe ( $t_{Fe}$ )/Cr ( $d_{Cr}$ )/MgO. We demonstrate that a light doping of Cr at the Fe/MgO interface enhances both the PMA and the VCMA coefficient. For an Fe thickness of 6.6 Å we observed an enhancement of the PMA from 0.68 MJ/m<sup>3</sup> to 1.03 MJ/m<sup>3</sup> when a 0.4 Å Cr layer was inserted between Fe and MgO. A value of the VCMA coefficient was enhanced from 230 fJ/Vm to 370 fJ/Vm for an Fe layer thickness of 5.9 Å as a result of a Cr insertion with a thickness of 0.7 Å.

## Experimental details

Fully epitaxial MgO (30 Å)/Cr (300 Å)/Fe ( $t_{Fe}$ )/Cr ( $d_{Cr}$ )/MgO (25 Å)/Fe (100 Å)/Ta (50 Å)/Ru (70 Å) multilayers (where the order is given from the bottom to the top of the sample) were grown on polished MgO(001) substrates under ultrahigh vacuum conditions (sample A). While the bottom ultrathin Fe wedge with perpendicular magnetic anisotropy was used as a free layer, the top Fe layer with an in-plane magnetization alignment was used as a reference in magnetotransport measurements. An MgO (30 Å)/Cr (300 Å)/<sup>57</sup>Fe (6 Å)/MgO (25 Å) heterostructure (sample B) was grown for the complementary Mössbauer spectroscopy studies, where the preparation procedure during a growth of four layer stack in sample B was the same as for the sample A, but no Cr doping was used at the Fe/MgO interface. After the MgO substrate was annealed, a Cr buffer layer was grown at 200 °C and annealed at 800 °C. A wedge-shaped Fe layer with a thickness  $t_{Fe}$  ranging from 3 Å to 7 Å was grown at 150 °C and annealed at 250 °C for 20 minutes. A sharpening of the reflection high-energy electron diffraction (RHEED) patterns was observed after annealing the thin Fe layer, which revealed an improvement of the crystalline quality as well as a smoothening of the annealed Fe surface. The Fe wedge was capped with a wedge-shaped Cr layer was prepared at room temperature with a thickness  $d_{Cr}$  ranging from 0 Å to 2 Å and with the Cr wedge gradient perpendicular to that of Fe (see Fig. 1). No change in the RHEED pattern was observed after deposition of the Cr-submonolayer on top of the Fe layer. Following Cr deposition, an MgO barrier was grown at room temperature and annealed at 350 °C. Finally, the top Fe layer was deposited and capped with the oxidation protective Ta/Ru bilayer prepared by sputtering. Rectangular pillars with areas of (2 × 6) μm<sup>2</sup> were fabricated on this sample using optical lithography, ion beam etching, and the lift-off process. Optical lithography was performed by a wafer stepper (Ultradtech Model1500) using double layer resists of LOR and AZ6124. Electrodes and MTJ pillars were etched by Ar ion milling using a Kaufman type ion source. SiO<sub>2</sub> was used as an insulator for MTJ pillars. Lift-off process was conducted by N-methylpyrrolidone and acetone under ultrasonic washer. As a result, a matrix of elements with different Fe and Cr thicknesses was formed. The tunneling magnetoresistance (TMR) was measured in the current-perpendicular-to-plane geometry (CPP) using the standard two-probe method under an in-plane external magnetic field on junctions with different Fe and Cr thicknesses. During a measurement, an in-plane magnetic field was applied parallel to the Fe [001] direction. For a fixed Fe thickness, we noted a gradual increase in the resistance-area (RA) product and a decrease in TMR along with an increase in Cr thickness at the Fe/MgO interface; for example, RA = 250 kΩμm<sup>2</sup> and TMR = 26% were noted for Cr/Fe/MgO at  $t_{Fe}$  = 5.9 Å, while RA = 312 kΩμm<sup>2</sup> and TMR = 13% were measured when 0.5 Å of Cr was inserted between Fe and MgO. Note that in the studied Fe thickness regime ( $t_{Fe}$  = (3–7) Å), the magnetization of the bottom Fe free (switchable) layer was aligned along the surface normal, while a direction of magnetization of the top reference (fixed) Fe layer was aligned in-plane along the easy-axis Fe [001] direction. When an in-plane magnetic field is applied, the magnetization of the free layer rotates towards its hard axis direction while the magnetization direction of the reference

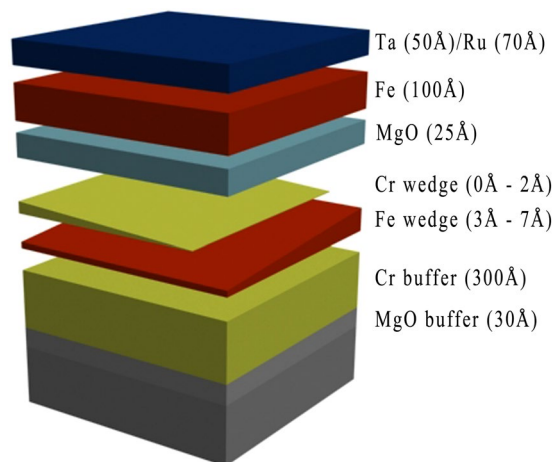


**Figure 1.** Schematic drawing of the magnetic tunnel junctions used in magnetoresistance measurements.

layer remains unchanged. Thus, the above-mentioned TMR values correspond to the relative orthogonal alignment between magnetizations.

Conversion electron Mössbauer spectroscopy (CEMS) measurements were performed for Cr/<sup>57</sup>Fe(6 Å)/MgO using a standard Mössbauer spectrometer equipped with a He/CH<sub>4</sub>-flow proportional detector and a <sup>57</sup>Co (Rh) source. The CEMS spectra were collected in the normal incidence geometry and fitted using Recoil software<sup>37</sup>. A Voigt-line based method was applied to fit the spectra, in which the distribution of the hyperfine parameters is represented by the sum of the Gaussian components<sup>38</sup>.

## Results

**Cr/Fe/MgO structure probed by Mössbauer spectroscopy.** As mentioned in the introduction, a post-deposition annealing of the Fe layer improves its surface quality. The role of the second annealing (after deposition of MgO) is to improve the crystallinity of MgO; however, it can affect the chemical and magnetic structure of Cr/Fe/MgO, especially at the interfaces. To verify the influence of the second annealing on the magnetic properties and chemical composition of Cr/Fe/MgO, a sample before annealing and a sample after annealing were compared. Figure 2 presents the CEMS spectra of Cr/<sup>57</sup>Fe (6 Å)/MgO collected for the sample before annealing (Fig. 2(a)) and the annealed sample after deposition of MgO (Fig. 2(b)). The nominal thickness of Fe corresponds to four atomic layers and, for an ideal film, one should expect a four-component spectrum reflecting Fe sites in different coordination. Instead, both spectra revealed a rather complex hyperfine pattern, which indicates a static long-range magnetic order and deviation from an ideal layered structure. The spectra were deconvoluted into two groups of magnetic sub-spectra that are distinct by isomer shifts (IS) and their correlations with the hyperfine magnetic field ( $B_{\text{hf}}$ ) distributions. The fit parameters are summarized in the Supplementary Information (Table 1). Sub-spectrum A (blue line) represents all of the Fe atoms except those at the Fe/MgO interface (nominally 3.4 atomic monolayers (ML)) and sub-spectra B and C (green and brown line respectively for the non-annealed and annealed samples) describe Fe atoms situated at the Fe/MgO interface, as judged based on the isomer shift value discussed below. Additionally, for the sample before annealing, a weak sub-spectrum P with small  $B_{\text{hf}}$  (site P) was identified (pink line). The key fit parameter for the magnetic sub-spectra was the intensity ratio ( $R$ ) of the second (or fifth) to the third (or fourth) line of the sextet components:  $R = I_{2(5)}/I_{3(4)}$ . The  $R$  value is determined by the angle  $\theta$  between the hyperfine magnetic field (local magnetization) and the  $\gamma$ -ray direction:

$$R = 4\sin^2\theta/(1 + \cos^2\theta). \quad (1)$$

For the given CEMS geometry (in which the  $\gamma$ -rays are parallel to the surface normal), the perpendicular ( $\theta = 0^\circ$ ) and in-plane ( $\theta = 90^\circ$ ) magnetization results in  $R = 0$  and  $R = 4$ , respectively.

Sub-spectrum A was decomposed into the smallest necessary discrete number of magnetic six-line Voigt components with the IS,  $B_{\text{hf}}$ , quadrupole interaction parameter ( $\epsilon$ ), and relative intensity as the fit parameters. The IS values of the components were linearly correlated with the hyperfine field, which is well justified for the Fe-Cr systems<sup>39</sup>. For both samples, the fits gave small  $\epsilon$  values, which is typical for cubic symmetry in metals. Moreover, the  $\epsilon$  is similar for all components in the non-annealed sample ( $\epsilon = (-0.026 \pm 0.004)$  mm/s) and is linearly correlated with  $B_{\text{hf}}$  for the annealed sample, which signifies a higher degree of structural order. The resulting  $B_{\text{hf}}$  distribution is well reproduced by a sum of Gaussian profiles whose width was fixed to 1.0 T for all components. The components identified for sub-spectrum A are attributed to Fe atoms with a different number of Cr neighbors. It was shown that for the Fe/Cr interface the  $B_{\text{hf}}$  of Fe atoms could be expressed by the following formula<sup>40,41</sup>:

$$B_{\text{hf}}(n_1, n_2) = B_{\text{hf}}(0, 0) + n_1B_1 + n_2B_2, \quad (2)$$

where  $B_{\text{hf}}(0, 0)$  denotes the hyperfine field of bulk Fe,  $n_1$ ( $n_2$ ) is the number of the nearest (next nearest) Cr neighbors, and  $B_1 = 3.19$  T ( $B_2 = 2.15$  T) is the contribution to the hyperfine magnetic field from one Cr atom in the first (second) shell around the Fe atom. Note that, because  $B_{\text{hf}}$  for Fe is negative, the Cr neighbors lower the absolute

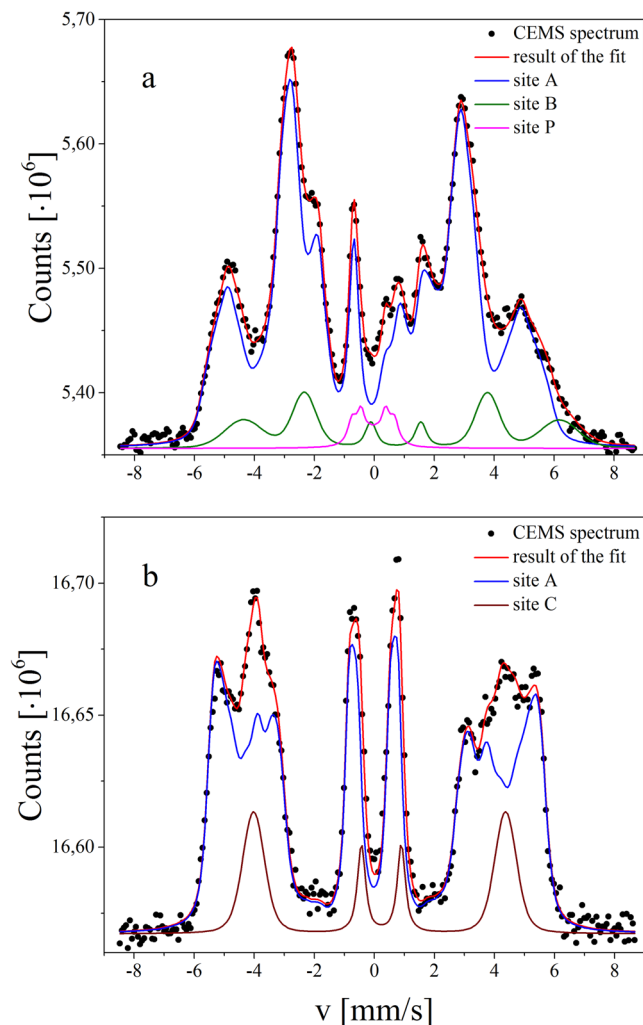


**Figure 2.** CEMS spectrum (black points) and result of the best fit (red line) of  $\text{Cr}/^{57}\text{Fe}/\text{MgO}$  collected for the sample before annealing (a) and the sample annealed at  $300^\circ\text{C}$  after deposition of  $\text{MgO}$  (b). The fits were deconvoluted into sub-spectra A (blue lines), B (green line), P (pink line) and C (brown line).

value of  $B_{\text{hf}}$  experienced by Fe atom, which means that higher Cr coordinations contribute to components with a smaller magnetic hyperfine splitting. Klinkhammer *et al.*<sup>39</sup> made a refinement of the formula (2) to account for an enhancement of the hyperfine field at the Fe/Cr interface. For ultrathin films,  $B_1$  and  $B_2$  may differ from the above values<sup>42</sup>, but the general trend that relates local coordination of Fe and  $B_{\text{hf}}$  is preserved.

To summarize, for an ideally flat and sharp Cr/Fe interface, only the hyperfine fields of atoms situated within the first and second layer from the Cr/Fe interface should be affected by the Cr proximity. Thus, only three components should be identified in the sub-spectrum A which contributes to about 85% of the total spectral intensity (nominally representing 3.5 ML):  $B_{\text{hf}}(4, 1)$  for the interface layer,  $B_{\text{hf}}(0, 1)$  for the layer next to the interface, and  $B_{\text{hf}}(0, 0)$  for deeper Fe sites. Instead, sub-spectrum A shows a multimodal  $B_{\text{hf}}$  distribution; 9 (Table 1, components A/1–A/9) and 7 (Table 1, components A/1–A/7) components were identified for the sample before and after annealing, respectively. The  $B_{\text{hf}}$  distributions  $P(B_{\text{hf}})$  are shown in Fig. 3, together with the IS of the components. In agreement with previous reports<sup>39</sup>, we observed a positive linear  $B_{\text{hf}}$  vs. IS correlation. This can be explained by an increase of s-electron density at the Fe nuclei with the increasing number of Cr neighbors.

Two groups of  $B_{\text{hf}}$  are distinctly resolved for the non-annealed sample (Fig. 3a). The low  $B_{\text{hf}}$  group is represented by components with  $|B_{\text{hf}}| < 25$  T (Table 1, components A/1–A/4), and the high- $B_{\text{hf}}$  group, which peaked at  $|B_{\text{hf}}| = 30.4$  T, contains components with  $|B_{\text{hf}}| > 25$  T (Table 1, components A/5–A/9). The relative intensity of the components with  $|B_{\text{hf}}| < 25$  T is 31%, which is equivalent to 1.3 ML of Fe. This group can be ascribed to the Fe atoms located in the vicinity of a diffused Fe/Cr interface. According to the Mössbauer studies of the Cr/Fe (40 Å)/Cr system, Fe atoms with the (4, 1) configuration should be described by  $B_{\text{hf}} = -23$  T for the sharp Cr/Fe interface<sup>39</sup>. Any deviation from the ideal, sharp interface, either configurational (steps or kinks) or chemical (interfacial Cr and Fe mixing), should lead to additional spectral components with  $B_{\text{hf}}$  slightly lower or higher than the ideal interfacial value. For example, an Fe atom diffused in the Cr-interfacial layer changes the configuration of four Fe atoms in the interfacial Fe layer to (3, 1) and one Cr atom in the interfacial Fe layer changes

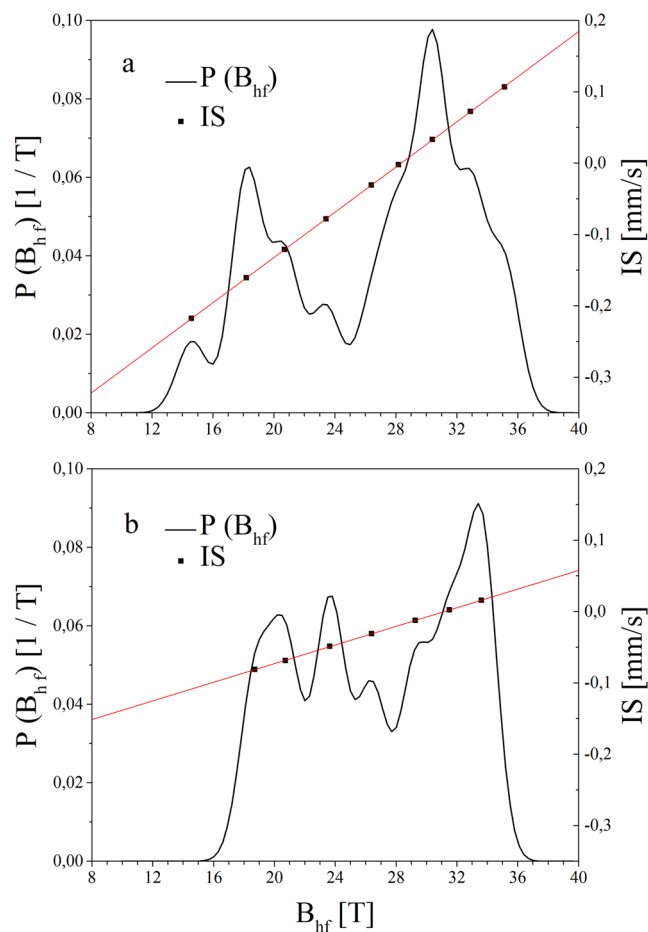


**Figure 3.** Hyperfine field distribution (black line) and the isomer shift (black squares) for the sample before annealing (a) and the sample annealed at 300 °C (b), linearly correlated to the hyperfine field distribution (red lines). The spectral intensity of the components and isomer shifts were shown on the left and right scale, respectively.

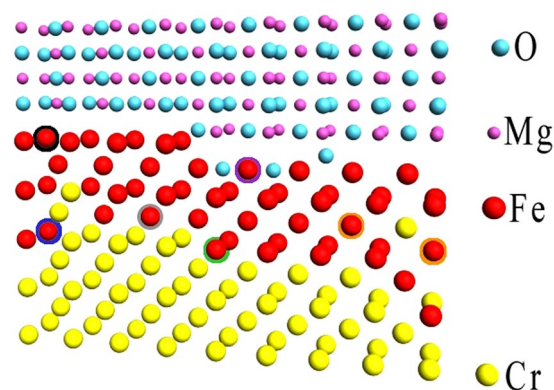


**Figure 4.** Model of Cr/Fe/MgO structure of showing interface Fe atoms at the specific interfacial sites. Yellow, red, blue and pink balls represents Cr, Fe, O and Mg atoms respectively. Examples of interfacial sites determined from CEMS spectra were marked by circles with different colors.

the configuration of four interfacial Fe atoms to (4, 2). On the other hand, since the Fe layer in our experiment is much thinner than the 40 Å Fe layer referenced above, a finite size reduction of magnetization and  $|B_{hf}|$  is obvious, we assign the component with a  $|B_{hf}| = 20.7$  T (Table 1, component A/3) to the atoms at the sharp interface with the (4, 1) configuration (Fig. 4, grey), in agreement with previous observations for ultrathin Fe (001) sandwiched between Cr<sup>42</sup>. Other components with  $|B_{hf}| < 25$  T (Table 1, components: A/1, A/2, A/4) are assigned to Fe atoms in the mixed interfacial Fe-Cr layers:  $|B_{hf}| = 18.2$  T and 23.5 T could correspond to the (4, 2) and (3, 1)

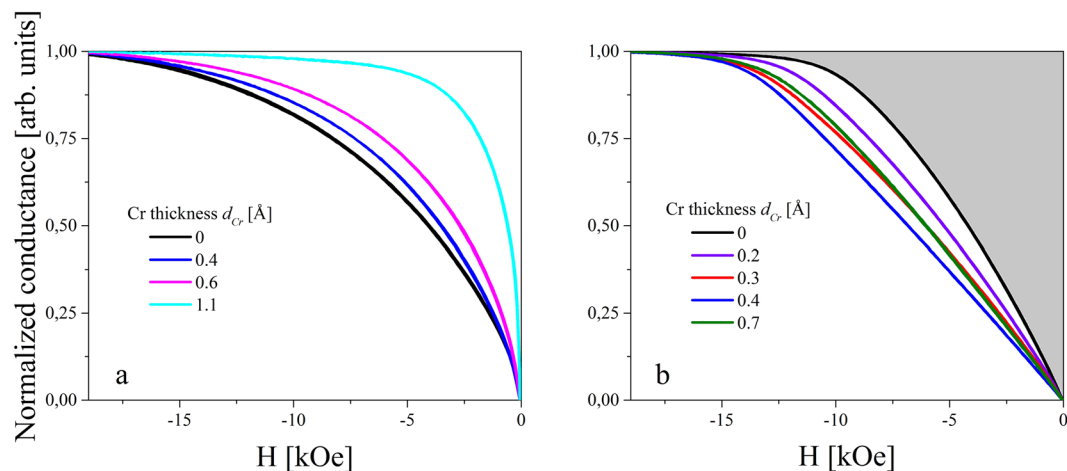


**Figure 5.** Normalized tunneling conductance obtained for Fe thickness of 5.1 Å (a) and 6.6 Å (b) for different Cr thicknesses.

configurations, respectively, which are characteristic not only for the mixed Fe-Cr layer but also for Fe atoms at steps or kinks (Fig. 4, green). Additionally, Fe atoms within a Cr-rich atomic interfacial layer (Fig. 4, blue) are responsible for the components with  $|B_{\text{hfl}}| < 15\text{T}$  (Table 1, component A/1); however, due to low intensity, their interpretation is less reliable. The weak sub-spectrum P can be associated to Fe atoms low-coordinated to other Fe atoms, located either at Fe/Cr or Fe/MgO interface, however due to the low intensity of the component P separation between two possible sites is ambiguous (Table 1, component P).

The second group of components with  $|B_{\text{hfl}}| > 25\text{T}$  constitutes 54% of the total spectral intensity, which is equivalent to 2.2 ML of Fe. The components with  $|B_{\text{hfl}}| = 26.4\text{T}$ , 28.2T, 30.4T, and 32.9T (Table 1, components A/5–A/8) are assigned to Fe configurations with  $n_1 + n_2 = 3, 2, 1$ , and 0, respectively, which can be found in the Fe layers next to the interface if some Cr atoms penetrate deeper into the Fe layer. (Fig. 4, orange). Finally, the component with the highest  $|B_{\text{hfl}}| = 35.1\text{T}$  and small positive IS relative to  $\alpha$ -Fe (Table 1, component A/9) is associated with Fe atoms in the sharp Fe/MgO interface (Fig. 4, black), where Fe retains its metallic character<sup>43</sup>. On the contrary, a small fraction of the Fe atoms, with strong bonds to the O atom in MgO (Fig. 4, violet), contribute to sub-spectrum B (Fig. 2(a), green), and are characterized by a distinctly positive IS =  $(0.61 \pm 0.03)$  mm/s that identifies an oxidation state of Fe (Table 1, component B). Two similar forms of Fe were found in the previous CEMS studies of the Fe/MgO interfaces<sup>44</sup>.

The character of the CEMS spectrum changes after annealing (compare Fig. 3(a) and (b)). In sub-spectrum A, two groups of the magnetic components are not as pronounced as those of the non-annealed sample. The relative weight of components with  $|B_{\text{hfl}}| < 25\text{T}$  (Table 1, after annealing, components A/1–A/3) is almost the same as for the non-annealed sample (33%); however, the component with  $|B_{\text{hfl}}| < 15\text{T}$  is no more present. The relative contribution of the component from Fe atoms in the (4, 1) configuration (11%) (Table 1, after annealing, component A/2) is higher than that for the sample before annealing (8%). Furthermore, an average hyperfine magnetic field of the components with  $|B_{\text{hfl}}| < 25\text{T}$  was increased from 19.4T before to 21.3T after annealing, which suggests a sharpening of the Cr/Fe interface. Also, the components associated with Fe atoms located further from the Fe/Cr interface are modified after annealing. First, a bulk-like component that corresponds to the (0, 0) configuration became more pronounced, and the metallic component with a high value of  $|B_{\text{hfl}}| = 35.1\text{T}$  (associated with a sharp Fe/MgO interface) (Table 1, component A/9) as well as the sub-spectrum B of an oxidic character (Table 1, component B) disappeared. Instead, sub-spectrum C with  $B_{\text{hfl}} = (-26 \pm 1.9)$  T and IS =  $(0.10 \pm 0.03)$  mm/s and the relative contribution of 16.5%, was recognized in a spectrum measured for the annealed sample (Fig. 2, brown) (Table 1, after annealing, component C). We interpret this sub-spectrum as originating from an interface formed by a mixed Fe–Cr atomic layer and MgO. Formation of such a layer can be understood if Cr segregation occurs during annealing. According to a simple thermodynamic consideration, Cr should segregate to the surface due to the higher surface energy of Fe compared to that of Cr<sup>45</sup>. First principle calculations revealed the complexity of the segregation process and showed that the segregation energy depends on Cr concentration and the surface orientation<sup>46</sup>. In particular, it was shown that the segregation of Cr impurities is favorable for the Fe (001) surface for an optimal Cr concentration within the Fe layer, which well explains the present case.

Sub-spectrum C has replaced the oxide-like sub-spectrum B in the non-annealed sample. This means that the Cr atoms at the Fe/MgO interface prevent formation of the oxide-like Fe–MgO bonds observed for the non-annealed sample. Furthermore, the component with  $|B_{\text{hfl}}| = 35.1\text{T}$  (Table 1, component A/9), which is of a metallic character and is interpreted as originating from Fe atoms at the sharp Fe/MgO interface, disappeared from the CEMS spectrum after annealing of the sample. This result is understandable if the presence of Cr at the Fe/MgO interface is considered; i.e. the hyperfine parameters at the Fe–Cr/MgO interface combine the properties of the sharp Fe/MgO interface and the influence of neighboring Cr atoms that lead to a reduction of  $|B_{\text{hfl}}|$ .

In short, the annealing has considerably changed the interfacial structure and the character of the Cr distribution in the Fe layer. Before annealing both interfaces were smeared and Cr tended to intermix and diffuse in the

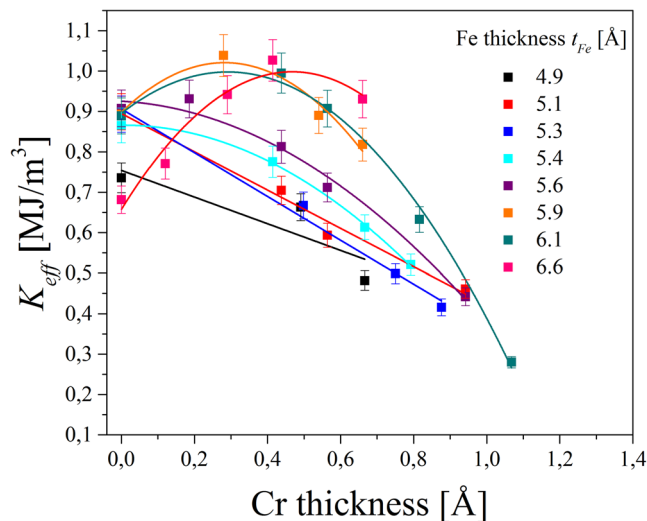


**Figure 6.**  $K_{eff}$  dependence on Cr thickness  $d_{Cr}$  for different Fe thicknesses. Straight lines and parabolas were fitted for  $K_{eff}(d_{Cr})$  dependence for  $t_{Fe} < 5.4 \text{ \AA}$  and  $t_{Fe} \geq 5.4 \text{ \AA}$ , respectively.

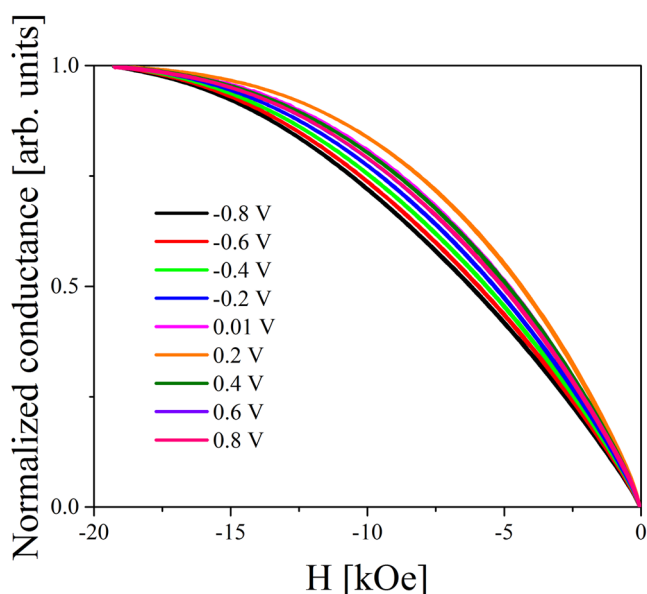


**Figure 7.** Exemplary normalized conductance curves obtained for an Fe thickness of 5.9 Å and Cr thickness of 0.5 Å measured under different bias voltages.

Fe layer. The annealing led to the configurational sharpening of the interfaces related to the Cr segregation and formation of a mixed Fe-Cr/MgO interface.

Together with the appearance of sub-spectrum C for the annealed sample, a striking change in the intensity ratio R was observed. While an in-plane magnetization alignment ( $R = 4$ ) is recognized before annealing, the magnetization aligns with the perpendicular direction after annealing ( $R = 0$ ). This suggests that a small Cr doping at the Fe/MgO interface is favorable for establishing the PMA in the Cr/Fe/MgO system.

This conclusion is significant in light of recent research on PMA and its VC in Cr/Fe/MgO<sup>32,33</sup>. As mentioned in the introduction, the maximum VCMA coefficient of about 290 fJ/Vm was observed for an Fe layer of nominal thickness of 5.3 Å, which is equivalent to 3.6 ML. This means that Cr impurities that segregate towards the Fe/MgO interface during annealing can be substantial for the MA and its VC in the system. To verify how a Cr insertion influences MA and its VC, systematic studies of the effective anisotropy and VCMA coefficient were performed for Cr/Fe ( $t_{Fe}$ )/Cr ( $d_{Cr}$ )/MgO as a function of different Fe and Cr thicknesses.

**Cr insertion dependence on PMA and its VC.** The effective magnetic anisotropy constants for different Fe and Cr thicknesses were determined from magnetoresistance measurements by using the method described in ref. 47. Examples of normalized conductance curves, which represent the in-plane component of the Fe layer

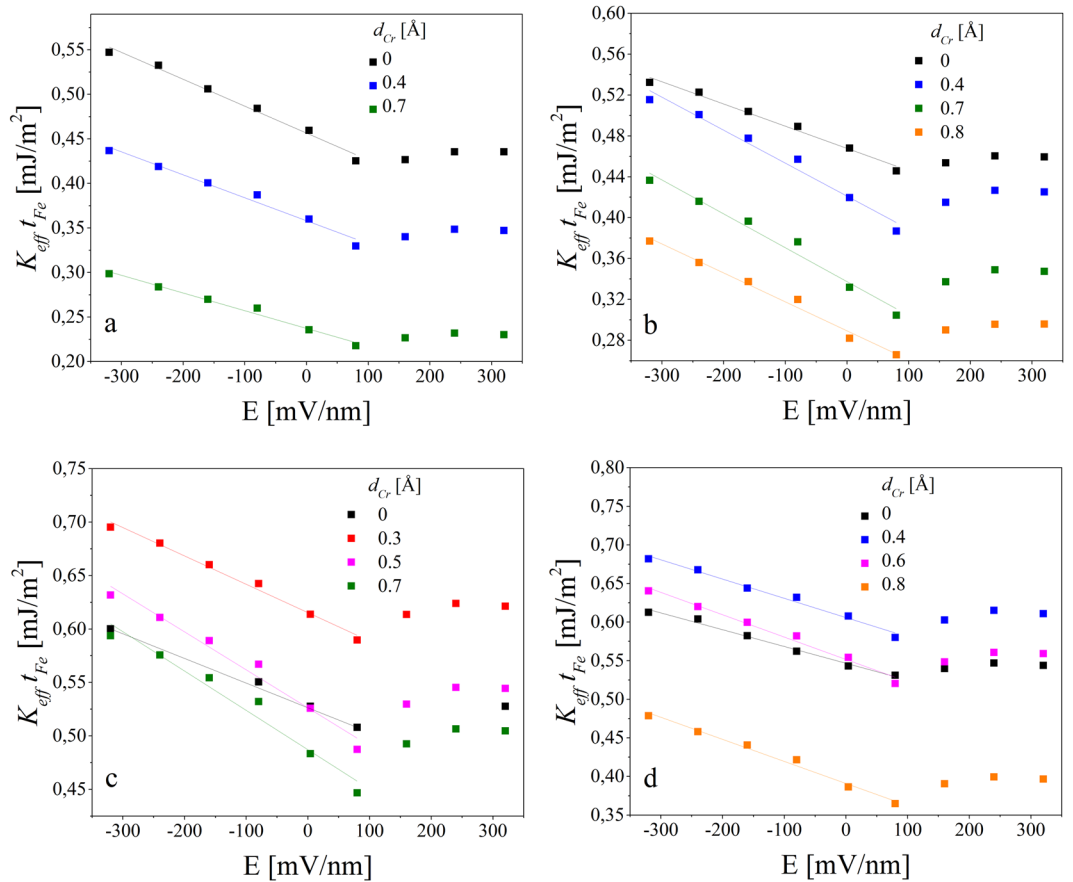


**Figure 8.**  $K_{\text{eff}} t_{\text{Fe}}$  vs. electric field dependence obtained for the Fe thickness of 5.1 Å (a), 5.4 Å (b), 5.9 Å (c) and 6.1 Å (d) for different Cr thicknesses (d). The slopes of linear fits indicate VCMA coefficients. Summary of VCMA coefficients were shown on Fig. 9.

magnetization, are shown in Fig. 5(a) and (b) for an Fe thickness of 5.1 Å and 6.6 Å, respectively, for different Cr thicknesses. The shaded area in Fig. 5(b) (shown as an example for  $d_{\text{Cr}} = 0$ ), when multiplied by  $M_s$ , is a measure of the PMA energy density. For an Fe thickness of 5.1 Å, we observed a gradual decrease of the saturation field ( $H_s$ ) when an ultrathin Cr layer was inserted at the Fe/MgO interface (Fig. 5(a)). On the contrary, for thicker Fe layers initially, for  $0.1 \text{ Å} < d_{\text{Cr}} < 0.4 \text{ Å}$ , we observed an increase in  $H_s$  with increasing Cr thickness at the interface (Fig. 5(b)). While a  $H_s = 15 \text{ kOe}$  was registered for  $d_{\text{Cr}} = 0 \text{ Å}$ , a saturation field of  $17 \text{ kOe}$  was obtained for  $d_{\text{Cr}} = 0.4 \text{ Å}$ . Further increase of  $d_{\text{Cr}}$  resulted in a decrease of  $H_s$ .

This suggests that while Cr doping at the Fe/MgO interface causes a reduction in PMA for very thin Fe layers ( $t_{\text{Fe}} < 5.5 \text{ Å}$ ), for thicker Fe films, it can contribute to an enhancement of PMA. Figure 6 summarizes a  $K_{\text{eff}}$  dependence on Cr thickness obtained for different Fe thicknesses, where a positive  $K_{\text{eff}}$  indicates an out-of-plane easy-axis of magnetization. The  $M_s$  values, which are necessary for the estimation of  $K_{\text{eff}}$  were obtained from SQUID measurements for selected Fe thicknesses. The  $M_s$  values for intermediate Fe thicknesses were determined from areal magnetization ( $M/S$ ) vs.  $t_{\text{Fe}}$  dependence. For the samples with Cr doping at the Fe/MgO interface, we used ( $M/S$ )( $t_{\text{Fe}}$ ) dependence obtained for different Fe thicknesses and a Cr layer inserted between Fe and MgO with a thickness of  $0.5 \text{ Å}$  (see: Supplementary Information).

Insertion of sub-monolayer Cr at the Fe/MgO interface induces substantial changes in the effective anisotropy in the Cr/Fe/MgO system. For  $t_{\text{Fe}} < 5.4 \text{ Å}$ , even  $0.5 \text{ Å}$  of Cr at the interface causes a decrease of positive effective magnetic anisotropy; the  $K_{\text{eff}}(d_{\text{Cr}})$  dependence can be described by straight lines in this Fe thickness regime. However, for thicker Fe layers sub-monolayer Cr doping leads to an enhancement of PMA. For  $t_{\text{Fe}} \geq 5.4 \text{ Å}$  the  $K_{\text{eff}}(d_{\text{Cr}})$  dependence is well reproduced by a quadratic function. This non-linear  $K_{\text{eff}}(d_{\text{Cr}})$  dependence can be related to the modification of magneto-elastic contribution to  $K_{\text{eff}}$ <sup>48</sup>. The Cr thickness for which a maximum value of  $K_{\text{eff}}$  was observed ( $d_{\text{Cr}}^*$ ) is shifted towards higher  $d_{\text{Cr}}$  values when the Fe thickness is increased. While a value of  $d_{\text{Cr}}^* = (0 \pm 0.01) \text{ Å}$  was obtained for  $t_{\text{Fe}} = 5.6 \text{ Å}$  from the fit a  $d_{\text{Cr}}^* = (0.5 \pm 0.3) \text{ Å}$  was determined for Fe thickness of  $6.6 \text{ Å}$  (the fit parameters are summarized in Supplementary Information (Table 2)). These results indicate that Cr doping at the Fe/MgO interface can be optimized for a maximum enhancement of PMA.

The VC of MA in the Cr/Fe/Cr/MgO system was studied by TMR measurements under different bias voltages, similar to our previous studies<sup>33</sup>. The effects of resistance and TMR ratio dependence on the bias voltage were eliminated through normalization of the TMR curves. The bias voltage was adjusted between the range  $-0.8 \text{ V} < U < 0.8 \text{ V}$ , which corresponds to the electric field range of  $-320 \text{ mV/nm} < E < 320 \text{ mV/nm}$  at the Fe/MgO



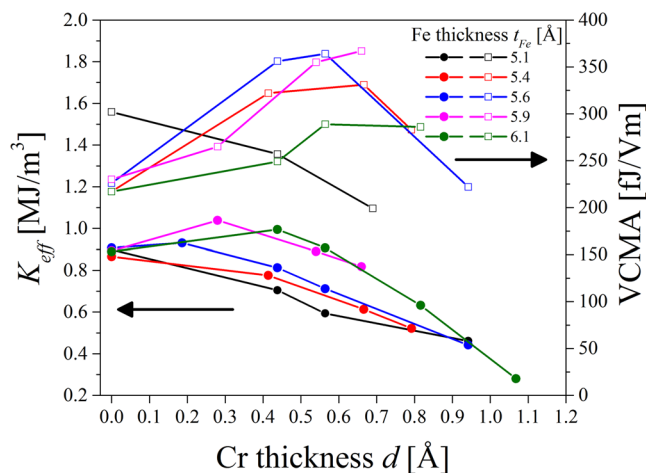


**Figure 9.** Effective anisotropy (filled circles, left scale) and VCMA coefficient (open squares, right scale) dependence on Cr thickness for different Fe thicknesses. The lines are guides to the eye.

interface. During measurements, we used a configuration in which a positive external voltage induces electron accumulation at the Fe/MgO interface. Figure 7 shows exemplary normalized conductance curves determined from the normalized TMR curves obtained for  $t_{\text{Fe}} = 5.9 \text{ \AA}$  and  $d_{\text{Cr}} = 0.5 \text{ \AA}$  under different voltages. For these Fe and Cr thicknesses, an electric field causes pronounced changes in the shape of the normalized conductance curve, which indicates a strong VCMA effect. Figure 8 presents a summary of the areal density of the anisotropy energy ( $K_{\text{eff}} t_{\text{Fe}}$  dependence on the electric field ( $E$ ) determined for Fe thicknesses of (a)  $5.1 \text{ \AA}$ , (b)  $5.4 \text{ \AA}$ , (c)  $5.9 \text{ \AA}$ , (d)  $6.1 \text{ \AA}$  for different Cr thicknesses inserted between Fe and MgO.

In agreement with our previous studies, for  $E < 100 \text{ mV/nm}$ , we noted a linear increase of  $K_{\text{eff}} t_{\text{Fe}}$  with an increase of negative electric field strength. For higher electric fields  $K_{\text{eff}} t_{\text{Fe}}$  increases nonlinearly with an increase of positive electric field, which indicates that in addition to the linear term, the second order electric field term should be considered in  $K_{\text{eff}} t_{\text{Fe}}(E)$  dependence for  $E > 100 \text{ mV/nm}$ . According to the theoretical predictions such behavior can be attributed to the existence of localized surface states in Fe layer, which may act as intrinsic charge-trapping sites and constitute a reverse point of the VCMA effect<sup>49</sup>.

For the thinnest Fe layers ( $t_{\text{Fe}} < 5.4 \text{ \AA}$ ), a gradual reduction of the slope in the  $K_{\text{eff}} t_{\text{Fe}}(E)$  dependence was observed together with increasing Cr thickness for  $E < 100 \text{ mV/nm}$  (compare black, blue and green data in Fig. 8(a)). In contrast, for thicker Fe layers, an insertion of Cr at the Fe/MgO interface results in an increase of the VCMA coefficient. An evident increase in the slope of the  $K_{\text{eff}} t_{\text{Fe}}(E)$  dependence was noted for  $t_{\text{Fe}} \geq 5.4 \text{ \AA}$  for optimal Cr doping (Fig. 8(b)–(d)). A summary of the VCMA coefficients determined for different Fe and Cr thicknesses is shown in Fig. 9 (open squares) together with the  $K_{\text{eff}}(d)$  dependence (filled circles). For the thinnest Fe layer of  $5.1 \text{ \AA}$ , a gradual decrease of the VCMA coefficient with increasing Cr thickness was found, from  $302 \text{ fJ/Vm}$  for  $d_{\text{Cr}} = 0 \text{ \AA}$  to  $257 \text{ fJ/Vm}$  for  $d_{\text{Cr}} = 0.4 \text{ \AA}$  and finally to  $199 \text{ fJ/Vm}$  for  $d_{\text{Cr}} = 0.7 \text{ \AA}$  (Fig. 9, black squares). For thicker Fe layers, an enhancement of the VCMA coefficient was observed for sub-angstrom Cr doping. The strongest influence of Cr on the VCMA was obtained for  $t_{\text{Fe}} = 5.6 \text{ \AA}$  and  $t_{\text{Fe}} = 5.9 \text{ \AA}$ . For an Fe thickness of  $t_{\text{Fe}} = 5.6 \text{ \AA}$ , we noted a VCMA coefficient of  $226 \text{ fJ/Vm}$  without Cr insertion, which was enhanced to about  $360 \text{ fJ/Vm}$  with Cr doping of  $0.6 \text{ \AA}$  (blue squares). For  $t_{\text{Fe}} = 5.9 \text{ \AA}$ , an enhancement of the VCMA coefficient from  $230 \text{ fJ/Vm}$  to  $367 \text{ fJ/Vm}$  was noted when a  $0.7 \text{ \AA}$ -thick Cr layer was inserted at the Fe/MgO interface (Fig. 6, pink squares). For a given Fe thickness, the Cr thickness for which a maximum VCMA coefficient was noted is shifted towards thicker Cr in comparison with the thickness for which a maximum  $K_{\text{eff}}$  was obtained. However, for some Fe thicknesses, a high  $K_{\text{eff}}$  and enhanced VCMA coefficient could be obtained by using Cr insertion. The highest value of the VCMA coefficient of  $367 \text{ fJ/Vm}$  was noted for an Fe thickness of  $5.9 \text{ \AA}$  and a Cr thickness of  $0.7 \text{ \AA}$ , for which  $K_{\text{eff}}$  was estimated to be  $0.8 \text{ MJ/m}^3$ .

As we shown in the experiment, an enhancement of  $K_{\text{eff}}$  and the VCMA coefficient could be obtained with a small amount of Cr doping at the Fe/MgO interface. However, the origin of the effect is unclear. The most probable cause is the Cr-impurities induced modification of the electronic structure of Fe. Modification of the band structure of Fe atoms at the Fe/MgO interface could affect both PMA and its VC. The impact of Cr impurities on the MA in Fe/MgO was investigated by Hallal *et al.* with a use of first-principle calculations<sup>50</sup>. They showed that PMA in the system can be enhanced due to the reduction of shape anisotropy, which prefers in-plane magnetization alignment. However, in our experimental studies we did not observe significant reduction of  $M_s$  for Cr-doped samples. Thus, enhancement of PMA obtained in our studies cannot be explained with reduction of shape anisotropy. Recent theoretical studies showed that the enhancement of PMA can be obtained if the valence charge at the Fe/MgO interface is optimized<sup>51</sup>. Zhang *et al.* obtained that PMA at the Fe/MgO interface increases with adding holes to the system as a consequence of an increase of electric field at the interface. After reaching a maximum, a gradual reduction of PMA was noted due to the reduced contribution from the  $d_{xy}$  orbitals. Because of a reduced number of the valence electrons in Cr in comparison with Fe, Cr insertion at the Fe/MgO interface could act as a hole doping at the Fe/MgO interface and its optimal concentration would lead to an enhancement

of PMA and VCMA. However, in the same paper the authors show that the doping of Fe with Cr is not the same as the rigid decrease of number of electrons in Fe, which might be attributed to the smaller electronegativity of the Cr atoms in comparison with Fe. Thus, a theoretical calculations that more accurately reproduce experimental conditions are still needed.

Finally, a change of a strain at the Fe/MgO interface due to the Cr doping could be responsible for enhancement of PMA and its voltage control. Although a big strain should not be expected in the system due to the small lattice mismatch between Fe and Cr (0.6%), recent ab-initio calculations showed that even small modification of the strain can dramatically affect the VCMA<sup>49</sup>.

In our experiment we can distinguish two Fe thickness regimes in which a different  $K_{eff}(d_{Cr})$  dependence were noted. While a decrease of  $K_{eff}$  as a function of  $d_{Cr}$  was obtained for a very thin Fe, an enhancement of  $K_{eff}$  was noted for an optimal Cr doping for thicker Fe layers. Analogically, two  $t_{Fe}$  regimes can be recognized for the VCMA( $d_{Cr}$ ) dependence. This indicates that for very thin Fe films the magnetic properties of MgO/Cr/Fe/Cr can be also influenced by the lower Fe/Cr interface. Especially, an increase of density of the Cr atoms close to the top MgO/Fe interface is expected due to the proximity of the lower Fe/Cr interface, which can determine magnetic properties in the system.

## Conclusion

In summary, we proved that sub-monolayer Cr insertion at the Fe/MgO interface could enhance both PMA and its electric field induced change. Similarly to our previous results, we noted an increase of PMA when a negative voltage was applied. Moreover, for  $t_{Fe} \geq 5.4 \text{ \AA}$  we showed that the change of  $K_{eff}$  under an electric field was more pronounced when a Cr layer was inserted at the Fe/MgO interface. This result, together with a detailed analysis of the chemical structure of the Cr/Fe/MgO system with the use of Mössbauer spectroscopy, shows that the presence of Cr at the interface may induce a strong VCMA effect.

## References

1. Brataas, A., Kent, A. D. & Ohno, H. Current-induced torques in magnetic materials. *Nat. Mater.* **11**(5), 372–381 (2012).
2. Huai, Y. Spin-transfer torque MRAM (STT-MRAM): Challenges and prospects. *AAPPS Bulletin* **18**, 6 (2008).
3. Amiri, P. K. *et al.* Electric-Field-Controlled Magnetoelectric Random Access Memory: Progress, Challenges, and Scaling. *IEEE Trans. Magn.* **51**, 11 (2015).
4. Matsukura, F., Tokura, Y. & Ohno, H. Control of magnetism by electric fields. *Nature Nanotechnol* **10**, 209 (2015).
5. Weisheit, M. *et al.* Electric field-induced modification of magnetism in thin-film ferromagnets. *Science* **315**, 349 (2007).
6. Maruyama, T. *et al.* Large voltage-induced magnetic anisotropy change in a few atomic layers of iron. *Nat. Nanotechnol* **4**, 158–161 (2009).
7. Chiba, D. *et al.* Electrical control of the ferromagnetic phase transition in cobalt at room temperature. *Nat. Mater.* **10**, 853–856 (2011).
8. Chiba, D. *et al.* Electric-field control of magnetic domain-wall velocity in ultrathin cobalt with perpendicular magnetization. *Nat. Commun.* **3**, 888 (2012).
9. Bernand-Mantel, A. *et al.* Electric-field control of domain wall nucleation and pinning in a metallic ferromagnet. *Appl. Phys. Lett.* **102**, 122406 (2013).
10. Schellekens, A. J., van den Brink, A., Franken, J. H., Swagten, H. J. M. & Koopmans, B. Electric-field control of domain wall motion in perpendicularly magnetized materials. *Nat. Commun.* **3**, 847 (2012).
11. Nawaoka, K., Miwa, S., Shiota, Y., Mizuochi, N. & Suzuki, Y. Voltage induction of interfacial Dzyaloshinskii–Moriya interaction in Au/Fe/MgO artificial multilayer. *Appl. Phys. Exp.* **8**, 6 (2015).
12. Shiota, Y. *et al.* Voltage-assisted magnetization switching in ultrathin Fe 80Co20 alloy layers. *Appl. Phys. Express* **2**, 3–6 (2009).
13. Shiota, Y. *et al.* Induction of coherent magnetization switching in a few atomic layers of FeCo using voltage pulses. *Nat. Mater.* **11**, 39 (2012).
14. Wang, W.-G., Li, M., Hageman, S. & Chien, C. L. Electric-field-assisted switching in magnetic tunnel junctions. *Nat. Mater.* **11**, 64 (2012).
15. Kanai, S., Yamanouchi, M., Matsukura, F. & Ohno, H. Electric field-induced magnetization reversal in a perpendicular-anisotropy CoFeB–MgO magnetic tunnel junction. *Appl. Phys. Lett.* **101**, 122403 (2012).
16. Nozaki, T. *et al.* Electric-field-induced ferromagnetic resonance excitation in an ultrathin ferromagnetic metal layer. *Nat. Phys.* **8**, 491 (2012).
17. Zhu, J. *et al.* Voltage-Induced Ferromagnetic Resonance in Magnetic Tunnel Junctions. *Phys. Rev. Lett.* **108**, 197203 (2012).
18. Wang, W.-G., Li, M., Hageman, S. & Chien, C. L. Electric-field-assisted switching in magnetic tunnel junctions. *Nat. Mater.* **11**, 64–68 (2011).
19. Pertsev, N. Origin of easy magnetization switching in magnetic tunnel junctions with voltage-controlled interfacial anisotropy. *Sci. Rep.* **3**, 2757 (2013).
20. Chiba, D. *et al.* Magnetization vector manipulation by electric fields. *Nature* **455**, 515–518 (2008).
21. Duan, C.-G. *et al.* Surface Magnetoelectric Effect in Ferromagnetic Metal Films. *Phys. Rev. Lett.* **101**, 137201 (2008).
22. Tsujikawa, M. & Oda, T. Finite Electric Field Effects in the Large Perpendicular Magnetic Anisotropy Surface Pt/Fe/Pt(001): A First-Principles Study. *Phys. Rev. Lett.* **102**, 247203 (2009).
23. Niranjani, M. K., Duan, C.-G., Jaswal, S. S. & Tsybal, E. Y. Electric field effect on magnetization at the Fe/MgO(001) interface. *Appl. Phys. Lett.* **96**, 222504 (2010).
24. Nakamura, K., Akiyama, T., Ito, T., Weinert, M. & Freeman, A. J. Electric Field-Induced Modification of Magnetocrystalline Anisotropy in Transition-metal Films and at Metal-Insulator Interfaces. *J. Magn.* **16**, 161 (2011).
25. Ibrahim, F., Yang, H. X., Hallal, A., Dieny, B. & Chshiev, M. Anatomy of electric field control of perpendicular magnetic anisotropy at Fe/MgO interfaces. *Phys. Rev. B - Condens. Matter Mater. Phys.* **93**, 1–5 (2016).
26. Bauer, U. *et al.* Magneto-ionic control of interfacial magnetism. *Nat. Mater.* **14**, 174 (2015).
27. Bauer, U., Przybylski, M., Kirschner, J. & Beach, G. S. Magnetoelectric charge trap memory. *Nano. Lett.* **12**, 1437–1442 (2012).
28. Rajanikanth, A., Hauet, T., Montaigne, F., Mangin, S. & Andrieu, S. Magnetic anisotropy modified by electric field in V/Fe/MgO(001)/Fe epitaxial magnetic tunnel junction. *Appl. Phys. Lett.* **103**, 062402 (2013).
29. Naik, V. B. *et al.* Effect of electric-field on the perpendicular magnetic anisotropy and strain properties in CoFeB/MgO magnetic tunnel junctions. *Appl. Phys. Lett.* **105** (2014).
30. Koo, J. W. *et al.* Large perpendicular magnetic anisotropy at Fe/MgO interface. *Appl. Phys. Lett.* **103**, 192401 (2013).
31. Lambert, C.-H. *et al.* Quantifying perpendicular magnetic anisotropy at the Fe-MgO(001) interface. *Appl. Phys. Lett.* **102**, 122410 (2013).

32. Kozioł-Rachwał, A. *et al.* The effect of the MgO buffer layer thickness on magnetic anisotropy in MgO/Fe/Cr/MgO buffer/MgO(001). *J. Appl. Phys.* **120**, 085303 (2016).
33. Nozaki, T. *et al.* Large Voltage-Induced Changes in the Perpendicular Magnetic Anisotropy of an MgO-Based Tunnel Junction with an Ultrathin Fe Layer. *Phys. Rev. Appl.* **5**, 044006 (2016).
34. Johnson, M. T., Bloemen, P. J. H., den Broeder, F. J. A. & de Vries, J. J. Magnetic anisotropy in metallic multilayers. *Rep. Prog. Phys.* **59**, 1409–1458 (1996).
35. Mirbt, S., Abrikosov, I. A., Johansson, B. & Skriver, H. L. Magnetic properties of Fe embedded in V and Cr: Thin films and dilute alloys. *Phys. Rev. B* **55**, 67 (1997).
36. Ravlić, R., Bode, M. & Wiesendanger, R. Correlation of structural and local electronic and magnetic properties of Fe/Cr(001) studied by spin-polarized scanning tunnelling microscopy. *J. Phys.: Condens. Matter* **15**, S2513–S2531 (2003).
37. RECOIL - Mössbauer Spectral Analysis Software for Windows, University of Ottawa, Ottawa. RECOIL (1998).
38. Lagarec, K. & Rancourt, D. G. Extended Voigt-based analytic lineshape method for determining N-dimensional correlated hyperfine parameter distributions in Mössbauer spectroscopy. *Nucl. Instr. Meth. B* **129**, 266 (1997).
39. Klinkhammer, F. *et al.* Interface roughness in Fe(100)/Cr film structures studied by CEMS. *J. Magn. Magn. Mater.* **161**, 49 (1996).
40. Landes, J. *et al.* Magnetic hyperfine fields near the Fe/Cr (100, 110) interface studied by CEMS. *J. Magn. Magn. Mater.* **86**, 71 (1990).
41. Dubiel, S. M. & Żukrowski, J. J. Mössbauer spectroscopy of Cr(110)/Fe(110)/Cr(110) sandwiches. *J. Magn. Magn. Mater.* **23**, 214 (1981).
42. Kubik, M., Ślęzak, T., Przybylski, M., Karaś, W. & Korecki, J. Interface modeling in Cr/Fe/Cr sandwiches studied by CEMS. *Vacuum* **63**, 337 (2001).
43. Kozioł-Rachwał, A. *et al.* Magnetism of ultrathin Fe films in MgO/Fe/MgO in epitaxial structures probed by nuclear resonant scattering of synchrotron radiation. *J. Appl. Phys.* **113**, 214309 (2013).
44. Młyńczak, E., Freindl, K., Spiridis, N. & Korecki, J. Epitaxial MgO/Fe(001) and Fe/MgO(001): Structures of the interfaces. *J. Appl. Phys.* **113**, 024320 (2013).
45. de Boer, F. R., Boom, R., Mattens, W. C. M., Miedema, A. R., and Niessen, A. K. *Cohesion in Metals North-Holland*, Amsterdam (1988).
46. Kiejna, A. & Wachowicz, E. Segregation of Cr impurities at bcc iron surfaces: First-principles calculations. *Phys. Rev. B* **78**, 113403 (2008).
47. Shiota, Y. *et al.* Quantitative Evaluation of Voltage-Induced Magnetic Anisotropy Change by Magnetoresistance Measurement. *Appl. Phys. Express* **4**, 043005 (2011).
48. Johnson, M. T., Bloemen, P. J. H., Broeder, F. J. A. & Vries, J. J. Magnetic anisotropy in metallic multilayers. *Reports Prog. Phys.* **59**, 1409–1458 (1996).
49. Ong, P. V. *et al.* Giant voltage modulation of magnetic anisotropy in strained heavy metal/magnet/insulator heterostructures. *Phys. Rev. B* **92**, 020407(R) (2015).
50. Hallal, A., Dieny, B. & Chshiev, M. Impurity-induced enhancement of perpendicular magnetic anisotropy in Fe/MgO tunnel junctions. *Phys. Rev. B - Condens. Matter Mater. Phys* **90**, 1–6 (2014).
51. Zhang, J., Lukashov, P. V., Jaswal, S. S., and Tsybal, E. Y. Elucidating the Voltage Controlled Magnetic Anisotropy, arXiv:1612.02724v1 [cond-mat.mtrl-sci].

## Acknowledgements

We thank T. Oda for fruitful discussions and E. Usuda for assistance with the experiments. This work was partly supported by ImPACT Program of Council for Science, Technology and Innovation, the Strategic AIST integrated R&D program, “IMPULSE”, and a Grants-in-Aid for Scientific Research (26709046). K. F. and J. K. were supported in part by the National Science Center (NCN), Poland (Grant No. 2011/02/A/ST3/00150).

## Author Contributions

A.K.-R. and T.N. designed the experiments and performed the sample fabrication, TMR measurements, and data analysis. S.Y. and Y.S. developed techniques for deposition, micro-fabrication, and measurements. K.F. and J.K. prepared samples for the Mössbauer spectroscopy (MS) studies and performed MS measurements and analysis. A.K.-R. wrote the manuscript with review and input from Y.S., J.K., and T.N. All authors contributed to the planning, discussion and analysis of this research.

## Additional Information

**Supplementary information** accompanies this paper at doi:10.1038/s41598-017-05994-7

**Competing Interests:** The authors declare that they have no competing interests.

**Publisher's note:** Springer Nature remains neutral with regard to jurisdictional claims in published maps and institutional affiliations.



**Open Access** This article is licensed under a Creative Commons Attribution 4.0 International License, which permits use, sharing, adaptation, distribution and reproduction in any medium or format, as long as you give appropriate credit to the original author(s) and the source, provide a link to the Creative Commons license, and indicate if changes were made. The images or other third party material in this article are included in the article's Creative Commons license, unless indicated otherwise in a credit line to the material. If material is not included in the article's Creative Commons license and your intended use is not permitted by statutory regulation or exceeds the permitted use, you will need to obtain permission directly from the copyright holder. To view a copy of this license, visit <http://creativecommons.org/licenses/by/4.0/>.

© The Author(s) 2017